A theoretical and experimental study of hexagonal molybdenum trioxide as dual-ion electrode for rechargeable magnesium battery

Marta Cabello, Alejandro Medina, Ricardo Alcántara, Francisco Nacimiento, Carlos Pérez-Vicente, José L. Tirado*

Departamento de Química Inorgánica e Ingeniería Química, Instituto Universitario de Investigación en Química Fina y Nanoquímica IUIQFN, Universidad de Córdoba, Campus de Rabanales, Edificio Marie Curie, E-14071 Córdoba, Spain.

*: E-mail: ralcantara@uco.es

Telephone: (+34) 957218568

ABSTRACT

The hexagonal polytype of molybdenum trioxide (h-MoO_3) was prepared through the hydrothermal method. The anisotropic growth of the particles yields to micro rods with prismatic geometry. Theoretical calculations were carried out to simulate the insertion of magnesium in the framework of h-MoO_3. The electrochemical behavior of single-phase h-MoO_3 in non-aqueous magnesium cells was studied, and for that purpose, Mg metal or activated carbon (A.C.) was used as a counter electrode. This is the first report about the insertion of a divalent cation into h-MoO_3. The experimental capacity vs. Mg is only around 20-50 mAh g^{-1}. Nevertheless, whether Mg metal is replaced by A.C. as the counter electrode, the electrochemical behavior of h-MoO_3 is improved, and the reversible capacity is about 100 mAh g^{-1} after 130 cycles. The combination of h-MoO_3 and A.C. forms a hybrid or asymmetric electrochemical capacitor. The mechanism of the reaction in the working electrode is more complex than a Mg^{2+}-insertion. Anion ($TFSI^-$) adsorption and redox of oxygen ions in the lattice of h-MoO_3 also contribute to the reversible capacity. Consequently, h-MoO_3 is a dual-ion electrode material. For higher mass ratio A.C./h-MoO_3, the experimental maximum reversible capacity is up to 350 mAh g^{-1} (equivalent to nominal composition $Mg_{0.94}MoO_3$).

KEYWORDS.

Magnesium batteries; post-lithium; supercapacitors; anion intercalation; computer simulations.

1

1. Introduction

One of the main scientific and technological challenges is to develop new systems to store electrical energy. For example, magnesium batteries could be very competitive in terms of energy density, natural abundance and safety compared to lithium ones. None of the rechargeable magnesium batteries reported in the literature is completely ideal yet. Unfortunately, finding host materials that can intercalate magnesium ions is much more difficult in comparison with lithium insertion materials, the chemistry behind magnesium insertion is not well understood and magnesium insertion or intercalation is a controversial topic [1-4]. The low compatibility between the most common electrolyte solutions and Mg metal is a drawback. Perchlorate ion, acetonitrile, and carbonates-based solvents form a blocking layer on Mg, while ethers are solvents more compatible with Mg [4, 5]. The high charge density and chemical hardness of Mg^{2+} cause strong interactions with the oxide ions in the framework, high activation energy for diffusion and sluggish kinetics. A way to resolve this drawback can be to use sulfides hosts instead of oxides, as it was proposed by Aurbach's group [6]. Another strategy could be shielding the charge of Mg^{2+} by solvation with certain molecules [2, 7]. The structural water previously intercalated in the electrode material could provide enhanced diffusion for the accommodation of cations and bonds that prevent structural degradation during electrochemical cycling [8, 9].

Irrespectively of the possible advantages of Mg compared to Li, a common way to achieve better cycling stability of the working electrode in magnesium cell is to replace the Mg counter electrode by an electrode based on carbon [3, 10, 11]. Throughout this strategy, one circumvents the poor electrochemical behavior of Mg

metal and can explore the insertion of magnesium ion in the working electrode. There are many papers in the literature about combining a (faradic type) cation-intercalating electrode with a (non-faradic type) anion-adsorbing carbon electrode and using lithium (or sodium)-based non-aqueous electrolyte [12, 13]. Several of the anions that can be intercalated or adsorbed are PF_6^-, BF_4^-, $TFSI^-$ and $AlCl_4^-$. Gunawardhana et al. proposed a new strategy and they studied lithium-intercalating α-MoO_3 anode vs. anion-intercalating graphite cathode [14]. Little attention has been paid to the role played by the activated carbon using a non-aqueous electrolyte based on a divalent cation such as magnesium. Likely to lithium supercapacitor with $TFSI^-$ anion described in the literature, it is expected that adsorption/desorption of anions ($TFSI^-$) and the electrical double layer contribute to the capacity of A.C. in a magnesium battery or in a hybrid battery-capacitor device.

The synthesis of $Mg_xMo_yO_z$ compounds by the ceramic method was first attempted as early as 1954 [15], and the only compound initially obtained of the Mg-Mo-O system was $Mg_2Mo_3O_8$ (hexagonal) [16]. In the 1990's decade, several Mg-Mo binary oxides with molybdenum reduced below Mo^{6+} were prepared and characterized, including α-$MgMoO_4$ (triclinic) [17]. Besides, molybdenum trioxide was proposed as a potential candidate for the electrode in rechargeable batteries, including magnesium batteries [10, 18]. Layered-type α-MoO_3 was studied as Mg-intercalating material [19] and expansion of the interlayer spacing was reported for $Mg_{0.5}MoO_3$ compared to pristine α-MoO_3 in the form of thin-film electrode [10], although the exact mechanism of the electrochemical reaction between MoO_3 and magnesium is still under discussion [2]. One of the ambiguities in the understanding of this electrochemical system is the exact rolled played by the electrolyte [20]. Another problem for the experimental study

of these magnesium batteries is to find an adequate reference electrode. There are five polytypes of MoO_3 [21-24]: orthorhombic α-MoO_3, monoclinic β-MoO_3, monoclinic β'-MoO_3, hexagonal h-MoO_3, and the high-pressure modification MoO_3-II. The thermodynamically stable phase is α-MoO_3, with the so-called double-layer planar structure (2D), and it has been much more extensively studied as an electrode for batteries [25]. However, the metastable polymorph h-MoO_3 possesses an open-structure (3D) with channels (~3.5 Å in diameter) that can contain mobile cations and it can be very suitable for insertion reactions. The tunnels in the structure of h-MoO_3 usually contain a small amount of ammonium cation and water molecules which come from the preparation route. The electrochemical behavior of h-MoO_3 in lithium cells has been reported [26, 27]. Recently, no electrochemical activity was experimentally found for layered-$Mg_2Mo_3O_8$ (space group $P6_3mc$) in magnesium cell, while chemical demagnesiation was successful but leads to destabilization of the parent lattice and amorphization [28]. The theoretical explanation of this result is based on the high activation barrier for magnesium diffusion in $MgMo_3O_8$.

The theoretical capacity of molybdenum trioxide is 372.3 mAh g^{-1} for 2 F mol^{-1} (Mo^{6+}/Mo^{4+}) or 1117 mAh g^{-1} for 6 F mol^{-1} (Mo^{6+}/Mo) and, consequently, it is worthy to study it. Thus, in this work, the main novelty is that the mechanism of the electrochemical reaction of h-MoO_3 in magnesium cell is explored by using both theoretical calculations and experiments by the first time, and for that purpose, both Mg metal and activated carbon (A.C.) are used as the counter electrode. It is found that the discharge/charge process is far from being a simple intercalation/deintercalation of magnesium.

2. Materials and methods

For the preparation of h-MoO_3, the hydrothermal method was followed [21, 24]. Firstly, 18.54 g of ammonium molybdate tetrahydrate $(NH_4)_6Mo_7O_{24}\cdot 4H_2O$) (Sigma-Aldrich, 99% purity) were dissolved in 50 mL of water. Secondly, 50 mL of 3 M $HClO_4$ were slowly added to the solution of molybdate while it was stirred to homogeneity. The resulting gel was aged for two weeks. The aged gel was transferred into a Teflon-lined stainless-steel autoclave, sealed, maintained at 180°C for 30 h and then cooled to room temperature. After the hydrothermal treatment, the resulting solid product was separated by centrifugation, washed with water and dried under vacuum at 100°C for 24 h.

The crystalline phases were characterized by X-ray diffraction (XRD). The XRD patterns were recorded using Bruker D8 Discover A25 equipment provided with CuKα radiation, Ge monochromator, and Lynxeye detector. The XRD pattern of the pristine h-MoO_3 phase was refined by the Rietveld method. The XRD patterns of electrodes at selected states of charge/discharge were obtained after opening the cells in the glove-box and protecting the samples with Kapton-tape, and the unit cell parameters of the phases were calculated using the full pattern matching method, as implemented in the commercial software Topas 4.2.

X-ray photoelectron spectroscopy (XPS) measurements were implemented in a SPECS Phoibos 150 MCD instrument, equipped with Al monochromatic source, to study the elements at the sample surface. The electrodes retrieved from the electrochemical cells for XPS measurements were previously rinsed with dry acetonitrile and dried under vacuum.

Infrared spectra were recorded using an FT-MIR Bruker Tensor instrument. For thermal analysis, a TGA/DTA Shimadzu instrument was employed, with a heating rate of five degrees per minute under a static air atmosphere. To study the particle morphology an SEM JEOL JSM 7800F apparatus was used, and the composition was analyzed by EDS detector coupled to this SEM apparatus.

EPR experiments were carried out on an X-band Bruker EMX-Micro spectrometer. The spectra were recorded at room temperature.

For the electrochemical experiments, two or three-electrode Swagelok-type cells were mounted in a glove-box filled with Ar. The three-electrode cell was T-shape. Whatman glass fibers discs impregnated with electrolyte solution were used as separators. The working electrode was MoO_3 (80%), carbon black (10%) and binder (PVDF, 10%) supported on Ti foil (Sigma-Aldrich). Magnesium (Sigma-Aldrich) or A.C. (Honeywell Fluka) were used as the counter electrode. The A.C. counter electrode can act as a quasi reference electrode with a potential of ca. 2.45 V vs. Mg [29]. When Mg was used as a counter electrode, another piece of Mg was used as a reference electrode. The A.C. was previously dried at 200°C under vacuum for one week, and after mixing with PVDF (10 %) it was deposited on Ti. The electrolyte solutions were prepared after drying the magnesium salt at 200°C under vacuum for 24 h and drying the solvents with a molecular sieve. Two electrolyte solutions were used. One electrolyte solution was 0.5 M $Mg(TFSI)_2$ (magnesium bis(trifluoromethanesulfonimide)) (Sigma-Aldrich,) in anhydrous dimethoxyethane (DME, Sigma-Aldrich, 99.5% purity). When using A.C. as a counter electrode, the employed electrolyte solution was 0.1 M $Mg(TFSI)_2$ in anhydrous acetonitrile (AN, Sigma-Aldrich, 99.8% purity).

For the geometry optimization and total energy calculations of the hypothetical intercalated phases, we used density functional theory (DFT) as implemented in the CASTEP software [30] (a full detailed description can be found in the S.I.). After the calculation of the energy (E) of the different phases, the average voltage (V) was calculated as:

$$V(Mg_{n-x}MoO_3/Mg_nMoO_3) = -\frac{\Delta G}{x\,e} = -\frac{E(Mg_nMoO_3)-E(Mg_{n-x}MoO_3)-x\,E(Mg)}{x\,e} \quad (1)$$

3. Results and discussion

3.1. Microstructure and composition

The structure of the as-prepared MoO_3 sample was studied by XRD (Fig. 1). The XRD pattern agrees well with the PDF number 21-0569 and it can be ascribed to single-phase h-MoO_3. For the Rietveld refinement of the XRD pattern, space group $P6_3/m$ (nº 176) was employed, and the starting atomic parameters were those published by Guo et al. [24]. Table S1 includes the refined structural parameters and reliability factors. The refined lattice cell parameters are a = 10.5523(9) Å and c = 3.7246(3) Å, in good agreement with the previous description of the structure [24]. The structure of h-MoO_3 (Fig. 1) is based in octahedral MoO_6 units, but the connection between the octahedra is different compared to α-MoO_3.

The SEM micrographs of the sample h-MoO_3 show that the particles are of micrometric size, with rod shape and hexagonal prism-like geometry (Fig. 2A, B). The hexagonal morphology of the particles reflects the crystallographic structure. The

diameter of the hexagons is ca. 5 μm and the length of the prisms is in the order of tens of microns. The individual prism-like microrods in some cases merge to form larger particles, indicating and assembly process. According to the X-ray microanalysis coupled to SEM, besides molybdenum and oxygen, there is a small amount of nitrogen in the sample. The approximate composition tentatively obtained from the microanalysis is $MoN_{0.04}O_{2.33}$, although this formula should be taken with caution because the quantification of light elements by X-ray microanalysis is not very adequate. The results of FTIR and thermal analysis can help to give a more adequate composition as it is discussed below.

The FTIR spectra are very important to characterize MoO_3 samples [23, 24, 31, 32] (Fig. 2C). The traces of water provide the bands at around 3600-3300 and at ca. 1620 cm^{-1} which are visible for h-MoO_3. Another characteristic feature of h-MoO_3 is the band at ca. 1400 cm^{-1} which can be assigned to bending vibration of H-N–H of ammonium ion (from the preparation method, as usually found in the literature). The band at ca. 3200 cm^{-1} is ascribed to ammonium vibrations. The bands in the range of 1000-400 cm^{-1} are assigned to O-Mo-O stretching and bending with different Mo-O bond lengths. The relatively sharp peak at ca. 975 cm^{-1} and the band at ca. 912 cm^{-1} are ascribed to the characteristic stretching vibrations of the Mo=O double bond in h-MoO_3. Other bands at 710, 600 and 520 cm^{-1} are attributed to Mo-O vibrations in h-MoO_3.

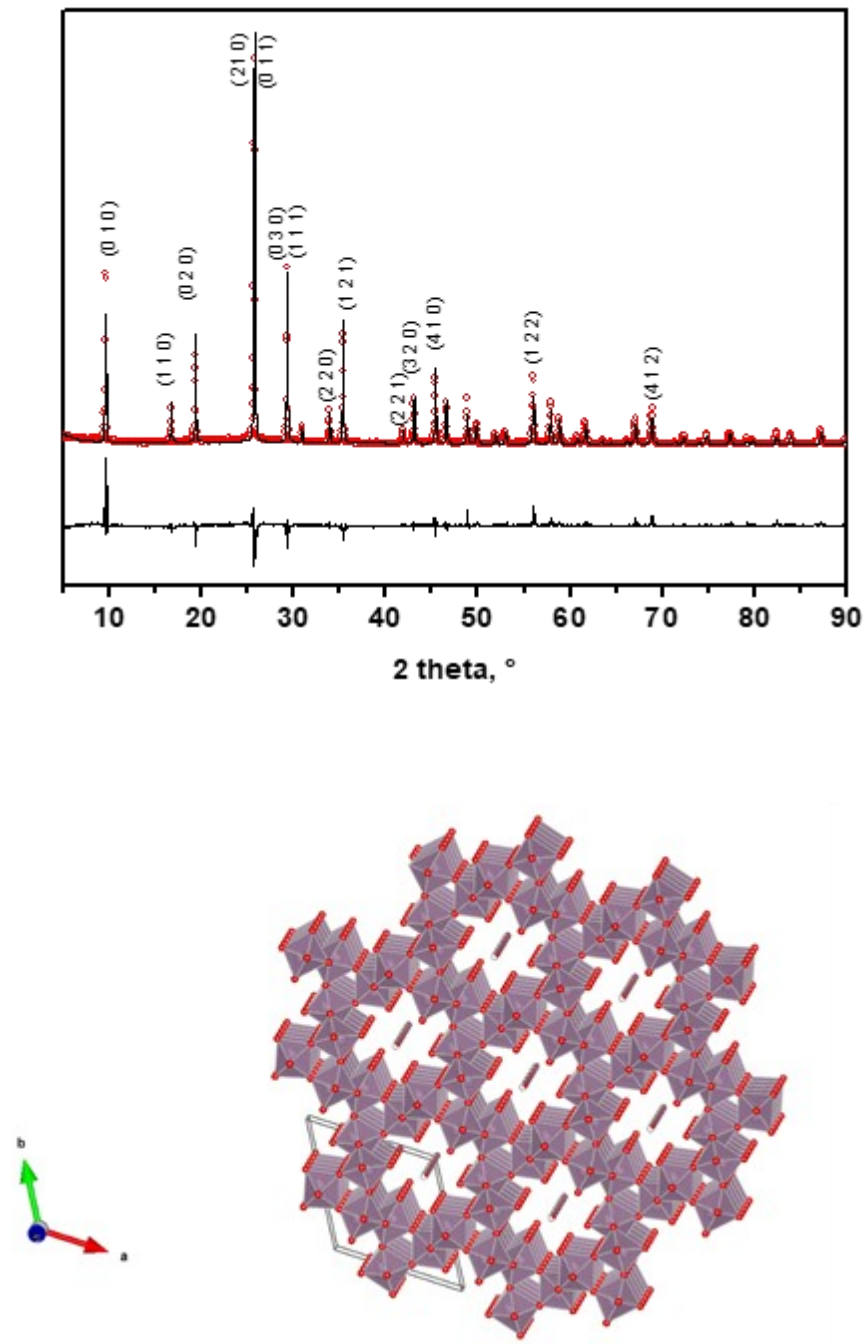

Figure 1. Top: Refined XRD pattern of h-MoO_3 by the Rietveld method. The Miller indexes of the most relevant Bragg reflections are shown. Bottom: projection of the structure in the ab plane, showing the tunnels of the structure along the c-axis. The octahedra represent the [MoO_6] units. The small circles inside the tunnels correspond to the theoretical position of O (from H_2O) and N (from NH_4^+) present in the structure.

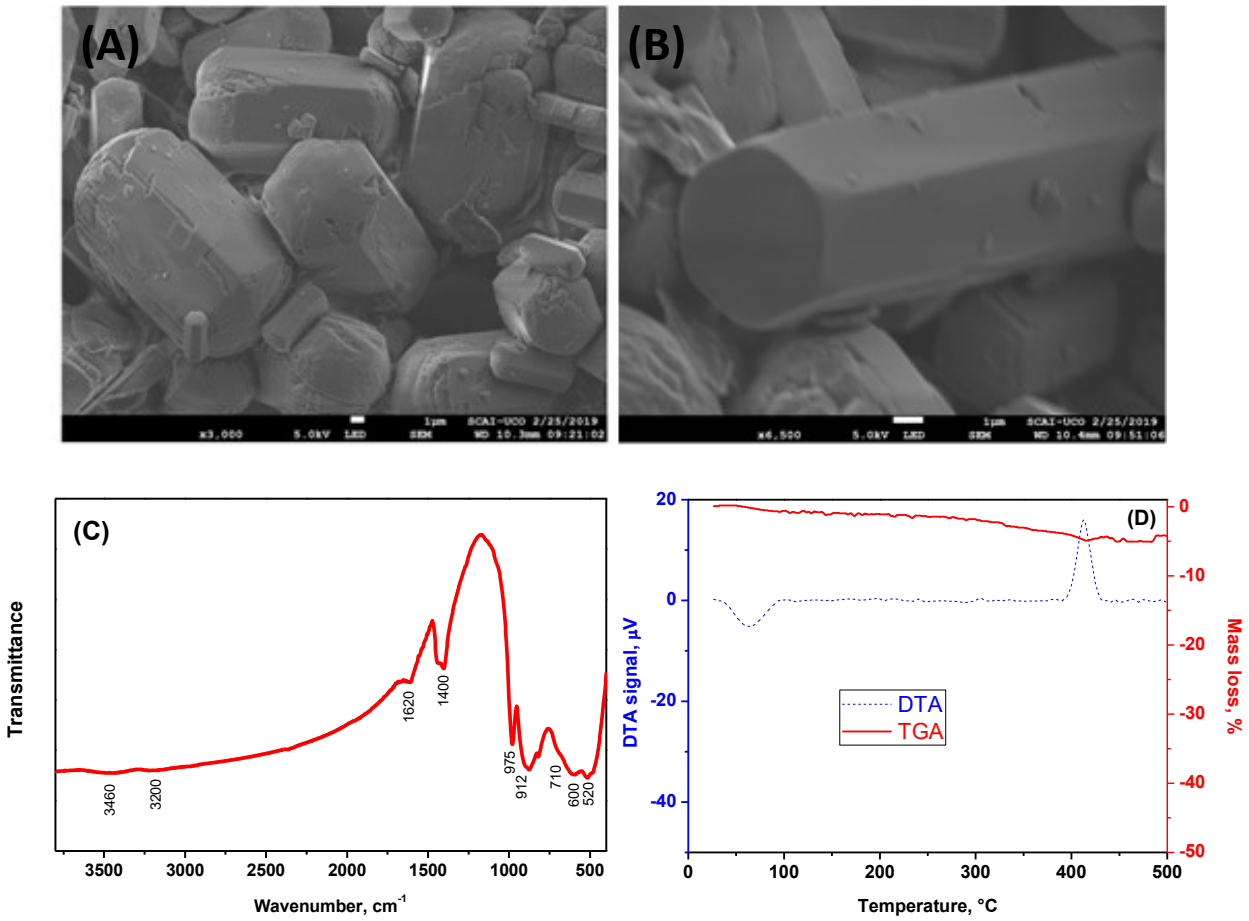

Figure 2. (A, B) SEM micrographs, (C) FTIR spectrum and (D) TGA/DTA results for h-MoO_3 sample.

The thermal behavior of the as-prepared sample h-MoO_3 was studied by simultaneous TGA/DTA measurement (Fig. 2D). The little mass loss (0.7%) observed before 90°C and the corresponding endothermal event can be ascribed to water physically adsorbed on the sample surface. There is an exothermal peak near 330-420°C with ca. 4% of mass loss that is ascribed to water and ammonium in the framework of h-MoO_3 and the concomitant transformation to α-MoO_3. According to the literature this compound is converted to α-MoO_3 at 420°C [21].

In conclusion, the results of XRD, FTIR, TGA/DTA and microanalysis of the as-prepared sample agree well with a composition of h-MoO_3 close to the formula previously in the literature ($((NH_4)_2O)_{0.09}\cdot MoO_3\cdot 0.3H_2O$) [21]. Also, it seems that the reasonable mechanism of the employed synthesis involves the dissolution of molybdate, re-precipitation in the form of hexagonal $((NH_4)_2O)_{0.09}\cdot MoO_3\cdot 0.3H_2O$ and particle growth in the crystallographic direction of the 6_3 axes.

4.2 Computational calculations for magnesium insertion into h-MoO_3

The structure of the h-MoO_3 can be described as parallel chains of edge-sharing [MoO_6] octahedral, assembled in groups of three by sharing a vertex, and forming trigonal prismatic holes potentially available for insertion. These groups are ordered in 3D to form large approximately hexagonal tunnels (Fig.1-bottom) which are also available for insertion. This phase is usually accompanied by the presence of large cations, such as NH_4^+ or K^+, that are in these tunnels [33, 34]. In the web page Materials Project the calculated results for orthorhombic $MgMoO_3$ were reported, the calculated average voltage for $MgMoO_3$ is 2.2 V [35], and the main theoretical difference after magnesiation is the expansion in the c-axis direction from 7.548 Å to 7.85 Å, while the

space group is preserved. However, to the best of our knowledge, there are no reports in the literature about divalent cations, such as magnesium, in h-MoO_3. The expected reaction of electrochemical insertion of magnesium can write as:

$$xMg^{2+} + 2xe^- + \text{h-}MoO_3 = \text{h-}Mg_xMoO_3 \quad (2)$$

We started by optimizing the structure of the h-MoO_3 phase assuming empty tunnels, before the inclusion of Mg in the structure. Then, different crystallographic sites were considered for locating the inserted Mg atoms: 2a, 2b, 2c, 2d, 4e, 4f, and 6h. The calculations showed that the most stable site for Mg insertion is the crystallographic site 6h, where the inserted atoms are located inside the tunnel, close to the octahedra defining that tunnel, as shown in Figure 3. It results in a stoichiometry $MgMoO_3$, with a reduction from Mo(VI) to Mo(IV). This insertion theoretically takes place at ca. 2.9 V vs Mg. Further reaction with Mg does not result in an additional Mg insertion, but in a conversion reaction, according to:

$$MgMoO_3 + 2\ Mg \longrightarrow Mo + 3\ MgO \quad (3)$$

We also analyzed the possibility of having ammonium and magnesium simultaneously in the structure. Firstly, we optimized the structure of $(NH_4)_{0.083}MoO_3$, and ammonium cations were placed in the tunnels, as previously described [24]. Then we tried the Mg insertion (for further details, see the S.I.). At the light of the previous results, we studied the insertion in the crystallographic site 6h. The average voltage of the reaction is ca. 2.7 V, slightly smaller than in the previous case. The calculated V-composition curve for Mg insertion is represented in Fig. 4. It is worth noting that the expected voltage for the Mg insertion in the hexagonal phase h-MoO_3 is somewhat higher than the voltage calculated by other authors for the orthorhombic phase α-MoO_3

(2.2 V) [35] and, consequently, the hexagonal phase could be advantageous for achieving higher energy density.

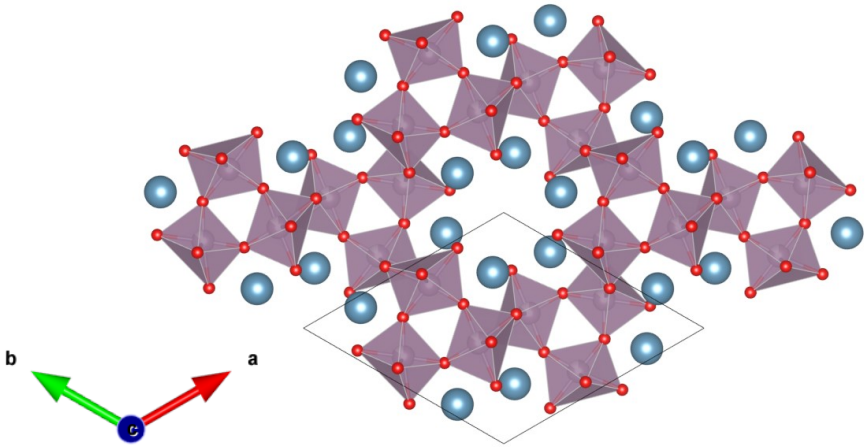

Figure 3. Structure of hexagonal MoO_3 and the possible site for Mg insertion. The octahedra represent the [MoO_6]. The blue circles correspond to Mg atoms in the crystallographic site 6h.

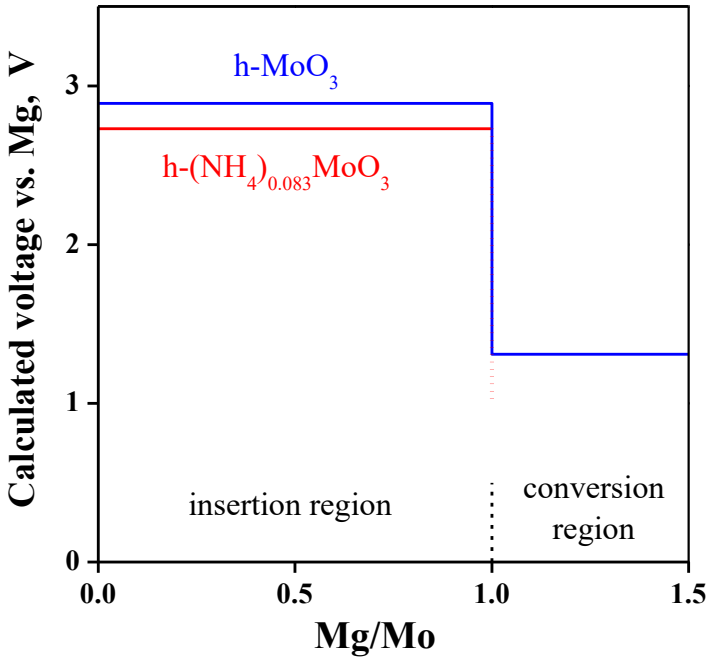

Figure 4. Calculated voltage profile for the reaction of h-MoO_3 with Mg.

4.3 Electrochemistry vs. Mg metal

The electrochemical behavior of the molybdenum trioxide sample was studied by carrying out experiments in magnesium cells using Mg metal (full Mg cell) or A.C. (half Mg cell) as the counter electrode. The electrochemical behavior of h-MoO_3 against Mg metal is poor, and the resulting capacity in the full Mg cell is only around 5-50 mAh g^{-1} which is equivalent to 0.013-0.13 Mg per Mo (Fig. 5). The average voltage is ca 0.9 V, which is lower than the voltage predicted by first-principles calculations for h-MoO_3, and lower than the voltage predicted by for Mg insertion in α-MoO_3 [35]. The voltage range of cycling is within the window of stability of the electrolyte (up to a maximum of 3.5 V) [36] and higher than the voltage for magnesium plating. The capacity in the first few cycles is higher for the AN solvent (ca. 50 mAh g^{-1}) (Fig. 5B) compared to DME solvent (ca. 5 mAh g^{-1}) (Fig. 5A), and this fact cannot be due to the higher concentration of magnesium in DME solution (0.5 M) compared to AN solution (0.1 M). Most probably it is due to the easier desolvation of magnesium from monodentate AN [37] compared to bidentate DME [36-38]. Thus, Aurbach´s group found that DME impedes magnesium intercalation into V_2O_5 due to strong solvation effects [39]. Recently, Attias et al. reported that $TFSI^-$ forms a layer on the surface of V_2O_5 that impedes magnesium intercalation [40]. On the other hand, it is known that the electrochemical activity of Mg metal is not very compatible with the AN solvent, due to electrolyte decomposition and formation of a non-conductive layer on the surface of Mg. After looking at these results, one could conclude that experimentally only a small amount of magnesium could be intercalated into h-MoO_3, in contrast to the theoretical calculations. The main reasons for the experimental low capacity could be the sluggish diffusion of magnesium, the low compatibility between the electrolyte solution and the

electrode materials, the formation of side-products on electrodes surface and the consequent impedance rise.

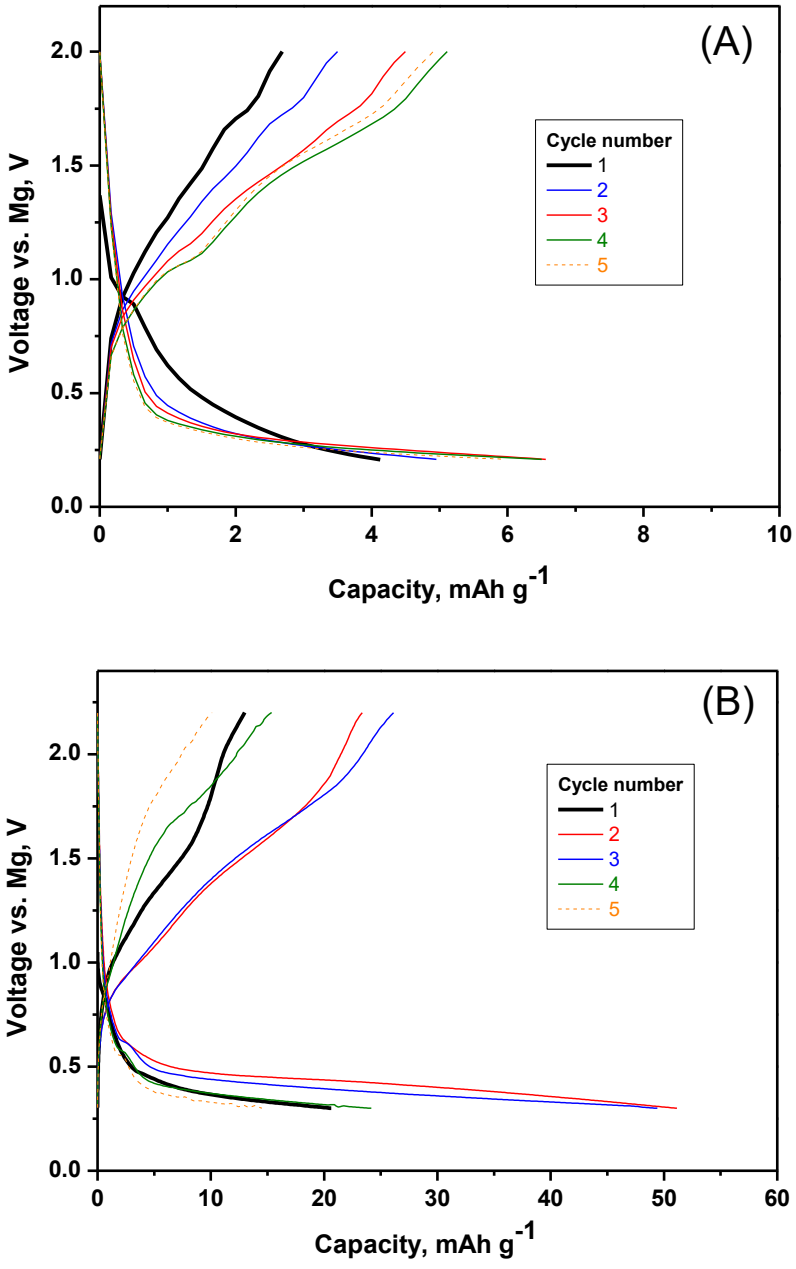

Figure 5. Results of galvanostatic experiments of h-MoO_3 in full magnesium cells, using Mg as a counter electrode, another Mg as a reference electrode, $Mg(TFSI)_2$ in DME (A) and AN (B) as the electrolyte solution. Current density: 10 mA g^{-1}.

According to the literature [26, 27], around two Li per Mo can be inserted into h-MoO_3 in the voltage range between 1.5 and 3.5 V vs. Li with no severe structure changes, although the site of lithium insertion has not been elucidated. With the further reduction, h-MoO_3 becomes amorphous at 0.9 V, and conversion to Mo metal and Li_2O occurs at 0.1 V. Compared to lithium, the experimental capacity to insert magnesium is smaller, unless under these experimental conditions. However, the capacity can be increased by changing the experimental conditions, for example by replacing Mg by A.C. in a half magnesium cell, as it is discussed below.

4.4 Electrochemistry vs. activated carbon

We have employed A.C. to replace the Mg electrode. The electrochemical device comprising h-MoO_3 and A.C. (half Mg cell) is rather a hybrid system battery/supercapacitor (Fig. 6). It is worth to note here that it has been previously reported that magnesium ion is reversibly adsorbed on A.C. electrode in hybrid battery-capacitor devices based on aqueous electrolytes [41]. In the voltage-capacity curves corresponding to molybdenum trioxide vs. A.C. (Fig. 6A, C) both curved and nearly linear profiles are observed, and this fact is characteristic of the hybrid battery/capacitor systems. Faradic process, non-faradic process, and cell polarization can contribute to the apparent electrochemical behavior. Irrespectively of the cell polarization, the A.C. electrode strongly improves the electrochemical cycling of h-MoO_3 compared to using the Mg electrode. The voltage range of this electrochemical system, between -1.5 V and +2.0 V, precludes its direct use in a commercial application, but these experiments serve for studying the reaction mechanism and unveiling new insights from post-lithium batteries. Thus, the voltage measured using A.C. can be correlated to the voltage vs. Mg by considering the open-circuit voltage of A.C. vs. Mg as it is currently found in the literature, although the voltage of A.C. is not constant during the charge/discharge. The

average discharge/charge voltage is ca 1.9 V vs. Mg. The discrepancy between the experimental voltage and the calculations can be due to the reaction mechanism, to the cell polarization and the change of A.C. potential. The capacity of the first discharge is ca. 60 mAh g^{-1} (equivalent to $Mg_{0.16}MoO_3$), and this capacity value can be ascribed to magnesium insertion into h-MoO_3 simultaneously to $TFSI^-$ adsorption in A.C. When the lower voltage limit is ca. -1.5V and the upper voltage limit is +1.5 V, the resulting reversible capacity is only around 35-50 mAh g^{-1}, but when after a few cycles, the imposed upper voltage limit is raised to +1.8 V the resulting capacity increases up to around 60-70 mAh g^{-1} (Fig. 6A, B). Analogously, the maximum reversible capacity of 90-180 mAh g^{-1} is observed for an upper voltage limit of +2.0 V (Fig. 6C, D). Interestingly, the capacity of the first charge up to 2.0 V vs. A.C. (ca. 188 mAh g^{-1}) is higher than the capacity of the previous discharge. Since there are not enough cations to be deintercalated from h-MoO_3 to sustain this charging capacity, this fact involves that the anion $TFSI^-$ is adsorbed in h-MoO_3 during the oxidation process. In this sense, there is a change of the slope in the voltage-capacity curve of the first charge after around 40-60 mAh g^{-1}, and it could be related to different reaction mechanisms. Firstly, at the beginning of the charging process in the region between -1.0 and +1.4 V, magnesium is deintercalated. In a second step, between +1.4 and +2.0 V, $TFSI^-$ is adsorbed in the h-MoO_3 working electrode and simultaneously removed from the A.C. counter electrode. These two voltage regions also are visible in the successive cycles (Fig. 6C). Thus, to achieve a reasonable specific capacity, the contributions of the two voltage regions are needed. In contrast to A.C., the Mg metal counter electrode does not adsorb a great amount of $TFSI^-$ and, consequently, the resulting capacity is higher using A.C. Irreversible electrolyte decomposition also could contribute to the charge capacity and the capacity loss upon cycling, particularly oxidation of $TFSI^-$ can contribute to the apparent capacity over ca. +1.4 vs. A.C. which is equivalent to ca. +3.8 V. against Mg.

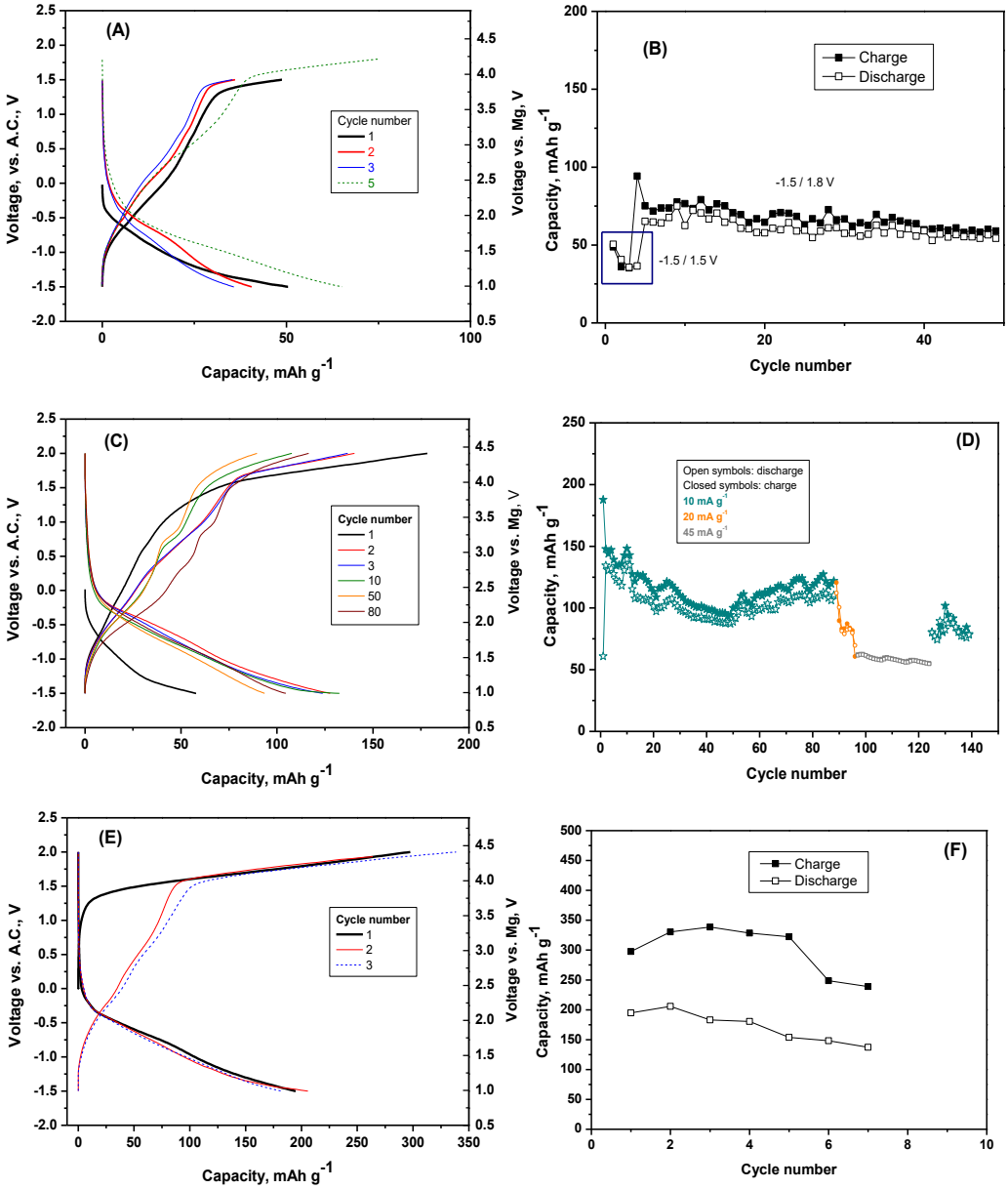

Figure 6. Electrochemical behavior of h-MoO_3 vs. A.C. for experiments starting in discharge (A-D) or starting in charge (D). Voltage capacity curves A, C, and E are shown on the left, and their respective capacity-cycle number plots B, D, and F are shown on their right, respectively.

If the electrochemical cycling begins directly by charging (Fig. 6E, F), the resulting capacity in the region between +1.4 and +2.0 V is 297 mAh g^{-1}, while the capacity is negligible below 1.4 V, and there is only a voltage region. This experimental capacity of the direct charge cannot be ascribed to any cation deinsertion but it must be due to anion adsorption (or absorption) and oxidation of the working electrode. After the first charge-discharge cycle, when magnesium also has been inserted into h-MoO_3 during the discharge, the second charge curve shows two voltage regions: cation deinsertion below 1.4 V and anion adsorption over 1.4 V. Thus, h-MoO_3 behaves as a dual electrode in which both cations and anions contribute to the capacity. The irreversible electrolyte decomposition at high voltage also can contribute to the apparent charge capacity, decreasing the Coulombic efficiency and driving to capacity fall upon cycling. The maximum discharge capacity is 200 mAh g^{-1}. Consequently, the charge capacity should be limited to achieve better cyclability.

In conclusion, the replacement of Mg by A.C. as a counter electrode does not only allow achieving the reversible charge/discharge process at the working electrode but also influences on the reaction mechanism of the working electrode, as it is further discussed below. The reaction mechanism was studied by using XPS and XRD of electrodes at selected states of charge.

4.5 XPS

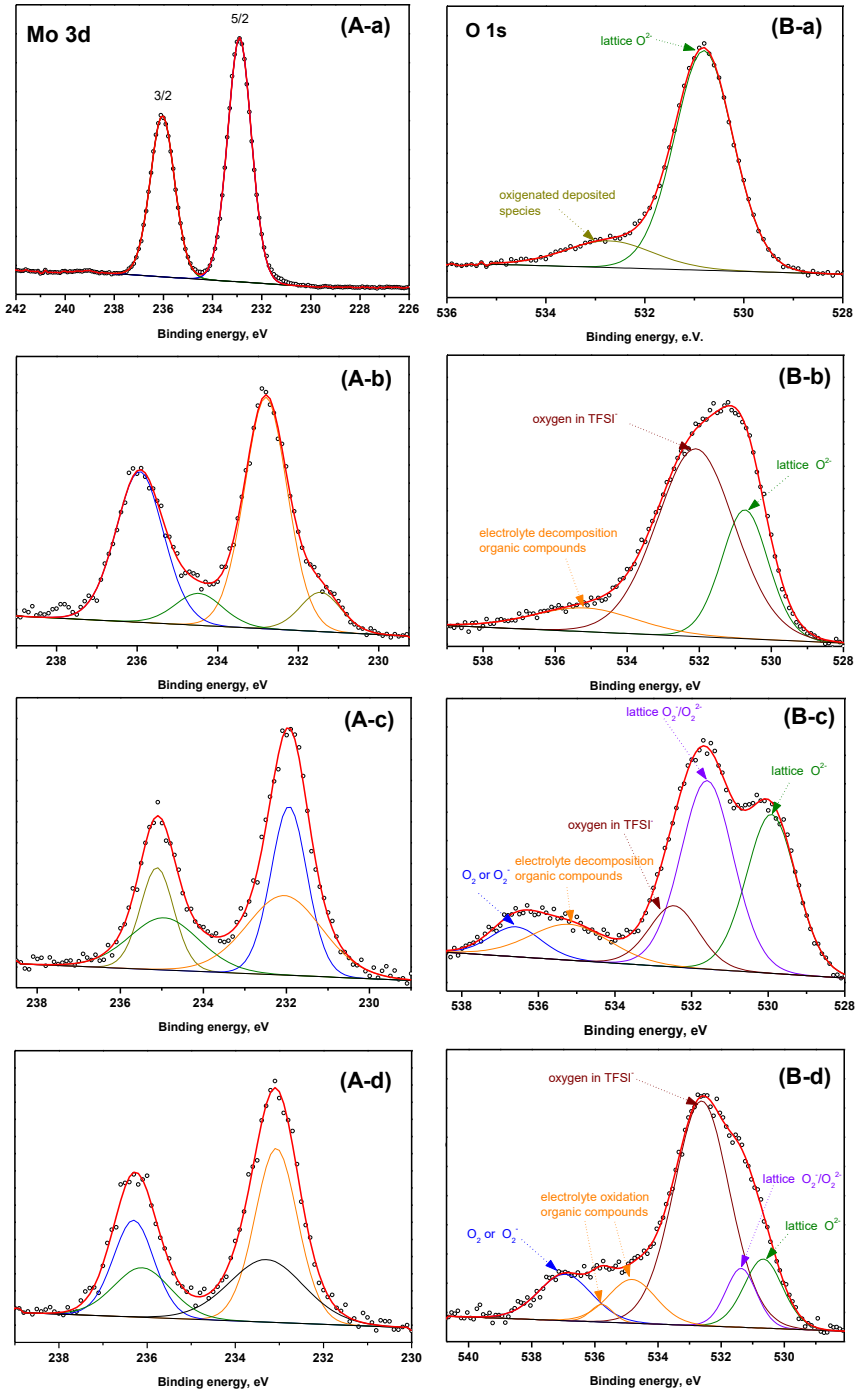

Figure 7. XPS in the regions of (A) Mo 3d and (B) O 1s for: (a) raw h-MoO_3, and (b) discharge (-1.5 V), (c) discharge (-1.5V)-charge (+2.0 V) and (d) charge (+2.0 V) electrode. For the sake of visibility, the scale of the x-axis is not the same for all the graphs.

XPS measurements were performed to study the valence state of molybdenum (Fig. 7A) and oxygen (Fig. 7B) atoms in the surface of the electrodes. For the raw h-MoO_3 sample, the spin-orbit doublet of Mo 3d is shown in Fig. 7A-a. The peaks of Mo $3d_{5/2}$ at 232.8 eV and Mo $3d_{3/2}$ 235.9 eV correspond to Mo^{6+} in stoichiometric MoO_3. The spin-orbit coupling splits the 3d core level into $3d_{3/2}$ and $3d_{5/2}$ with splitting energy of 3.1 eV. The O 1s peak is comprised of two contributions. The major component at 530.7 eV corresponds to oxide ion ($O^{=}$) in the framework of MoO_3, and the minor component at 532.6 eV corresponds to oxygen species adsorbed on the surface of MoO_3. The binding energy difference ΔB.E.(O1s − $Mo3d_{5/2}$) = 297.9 eV agrees well with Mo^{6+} [25,42].

After the first discharge of h-MoO_3. to -1.5 V vs. A.C, besides the doublet of Mo^{6+} two new components of smaller intensity were used for the fitting of the spectrum in the region of Mo 3d (Fig. 7A-b). These two new components are due to a partial reduction from Mo^{6+} to Mo^{4+}. Three oxygen species contribute to the spectrum in the O 1s region (Fig. 7B-b): oxide in the framework of MoO_3 (Mo-O at 530.8 eV), oxygen in $TFSI^-$ (S-O at 532.2 eV), and oxygen in organic compounds (C-O at 535.3 eV). Similarly, Sun et al. found $TFSI^-$ chemically bonded to manganese dioxide electrode that could not be removed by washing with solvent [43]. The binding energy difference between the minor component of molybdenum and oxide in the lattice, ΔB.E.(O1s − $Mo3d_{5/2}$) = 299.2 eV, agrees well with the presence of Mo^{4+}. These results involve that the first reduction process yields to some reduction of Mo^{6+} to Mo^{4+} and the formation of a surface layer on the particles of h-MoO_3. This surface layer contains electrolyte and products of electrolyte decomposition.

The XPS results after the first discharge-charge cycle are displayed in Fig. 7A-c for Mo 3d and in Fig. 7B-c for O 1s. The O 1s core level of the oxidized electrode markedly changes compared to the raw material and compared to the reduced electrode. The spectrum for the cycled electrode becomes more broadened and it must be fitted with five components placed at 536.6, 535.2, 532.5, 531.6 and 529.9 eV, respectively. The peak at higher binding energies (536.6 eV) tentatively could be ascribed to adsorbed dioxygen [44,45] or superoxide O_2^- [46]. Oxygen in organic compounds contributes to the peak at 535.2 eV. The O 1s peak of $TFSI^-$ anion appears at 532.5 eV. The large peak at 531.6 is ascribed to $O^-/O_2^=$ [47]. The peak at 529.9 eV is due to $O^=$ in the crystalline network. In the region of Mo_{3d} (Fig. 7A-c), the doublet is more broadened compared to raw h-MoO_3, which indicates several types of molybdenum; and the peaks are slightly shifted toward lower binding energies, corresponding to higher electronic density. Four peaks were used for the fitting, located at 235.1, 234.9, 232.0 and 231.9 eV. Rather than the position of the Mo 3d peaks, it is more significant the fact that the binding energy difference from O^{2-} in the lattice, $\Delta B.E.(O1s - Mo3d_{5/2})$ = 298.0 eV is the same than that of raw h-MoO_3, and it corresponds to Mo^{6+}. Thus, it is concluded that both molybdenum and oxygen atoms participate in the redox processes during the charge/discharge. Most probably, molybdenum atoms interact with the $TFSI^-$ anion and the spectrum of Mo 3d is affected for that interaction.

The spectra after the direct charge (no previous discharge) are shown in Fig, 7 A-d, and B-d. Six peaks were used for fitting the region of O 1s core level which corresponds to several oxidation states and covalence. The peak placed at lower binding energy, centered at B.E=530.7 eV is due to O^{2-} in the Mo-O framework). Oxygen from the electrolyte and oxidized forms of oxygen also contribute to the spectrum. In Figs. 7B-c and d, the contribution of oxygen in $TFSI^-$ is lower while the contribution of

oxygen in organic compounds of decomposed electrolyte is higher compared to Fig. 7B-b Thus, the oxidation of O^{2-} to O_2^-/O_2^{2-} in h-MoO_3 is accompanied by electrolyte decomposition on the electrode surface at the end of the charging process. In the region of Mo 3d, the spectrum of the charged electrode (Fig. 7Ad) is very similar to raw h-MoO_3 but more broadened, suggesting certain strain in the framework.

As a conclusion, the surface of the charged electrodes unambiguously contains oxygen atoms in a more oxidized form that raw h-MoO_3 and that the discharged electrode. These results involve that the redox activity of oxygen to compensate for the charge of $TFSI^-$ adsorption yields to oxidation from oxide to peroxide and superoxide. It is worthy to note here that Guo et al. reported that hexagonal molybdates release oxygen gas through oxidation with Ce^{4+}(aq.) while molybdenum remains in the Mo^{6+} state following this reaction

$$(A_y \cdot zH_2O)Mo_{6-x}O_{18-x}(H)_{4x-y} \xrightarrow{-H_2O,-O_2} A_yMoO_3 \quad (4)$$

in which A is a univalent cation [24]. Similarly to this chemical oxidation, the oxidation from oxide to superoxide or peroxide in the electrochemical cell probably is an intermediate state before O_2 evolution at higher potentials.

4.6 EPR

Electron paramagnetic resonance (EPR) is a technique very suitable to study paramagnetic centers diluted in a diamagnetic matrix, such as reduced molybdenum ions (Mo^{5+}-$4d^1$) and oxygen radical species in MoO_3 [48]. The EPR spectra of uncycled and cycled h-MoO_3 electrodes are shown in Fig. 8. Pristine h-MoO_3 posses an EPR signal of small intensity centered at g=2.003 which is ascribed to paramagnetic defects, such as an electron trapped in an oxygen defect [49-51]. In the electrode comprising active material (h-MoO_3), conductive agent (carbon black) and binder (PVDF), the

small signal of Mo^{5+} centers is masked by the intense signal of paramagnetic centers in the carbon phase [52]. The electrode retrieved from the electrochemical cell after discharge to -1.5 V vs. A.C. also exhibits an EPR line dominated by a paramagnetic center in the carbon phase at g=2.00, and other contributions (Mo^{5+} and Mo^{4+}) are not very well detected. Nevertheless, the asymmetric line of low intensity which visible at a higher magnetic field and near g=1.9 can be indicative of the occurrence of new paramagnetic centers of molybdenum in axial symmetry. The reduction of the intensity of the EPR signal in the reduced electrode also was previously observed in carbon electrodes employed in lithium and sodium cells [52]. However, after the first discharge(-1.5V)/charge(+2.0V) cycle, irrespectively of the high-intensity signal of the carbon phase, the EPR becomes much more complex due to the contribution of new paramagnetic centers created by the charge of the electrochemical cell. Several anisotropic lines are observed near g =2.15, 2.09, 1.93 and 1.88, and other signals may overlap with carbon signal, which are ascribed to oxygen radical species, typically O_2^- and O^- [48,53], while the fraction of O_2^{2-} is diamagnetic and it can explain the weakness of the signal due to paramagnetic oxygen. Henceforth, the EPR results agree well with the XPS results and anionic redox.

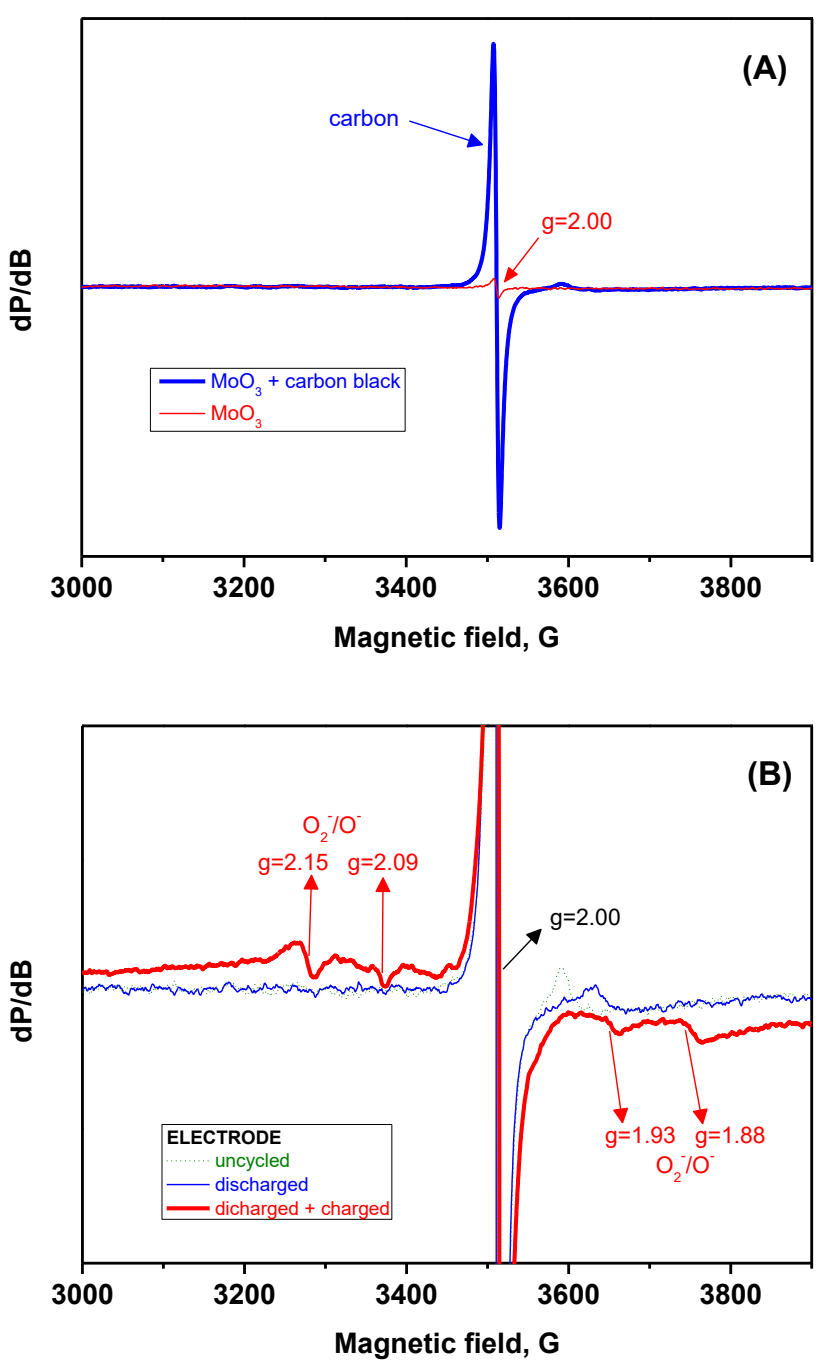

Figure 8. EPR spectra. (A) A general view of spectra for pristine h-MoO_3 and uncycled electrode (h-MoO_3 + carbon + PVDF). (B) Detailed view for uncycled electrode, after the first discharge and after the first discharge-charge cycle.

4.7 XRD

Ex-situ XRD patterns of the magnesiated electrodes of h-MoO_3 were used to explore the mechanism of the electrochemical reaction (Fig. 9). The structure of h-MoO_3 is preserved during the electrochemical cycling, and the same space group can be used for indexing all the electrodes at different sates of charge-discharge. The phase $Mg_2Mo_3O_8$ is not formed. During the first two discharge/charge processes, irrespectively of the state of charge, the lattice cell parameters remained nearly unchanged (Table 1). Expansion of the interlayer upon discharge was reported for orthorhombic α-MoO_3 in magnesium [10], calcium [25] and lithium [54]. Guo et al. reported that empty h-MoO_3 exhibits only slightly larger a-axis compared to the material chemically intercalated with monovalent cations [24]. The small change of the lattice found in h-MoO_3 could be an advantage compared to α-MoO_3. The dual uptake of cations and anions could contribute to the overall stabilization of the lattice through the balancing of the electrical charges. The adsorption of $TFSI^-$ and the consequent film formation can impede, or slow down, the diffusion of magnesium into h-MoO_3. The XRD pattern of the discharged electrode retrieved form the electrochemical cell after 67 cycles (Fig. 8f) shows broadening of the reflections towards lower angles, and the resulting lattice cell parameters indicate that the cell is slightly expanded in both *a* and *c* axis (Table 1), suggesting that with further cycling, a limited true (co)insertion of anions and/or solvent molecules could occur. The formation of new defects, such as oxygen defects, also could contribute to lattice expansion, microstrains, loss of crystallinity, broadening of the XRD reflections and finally capacity fade and battery fail.

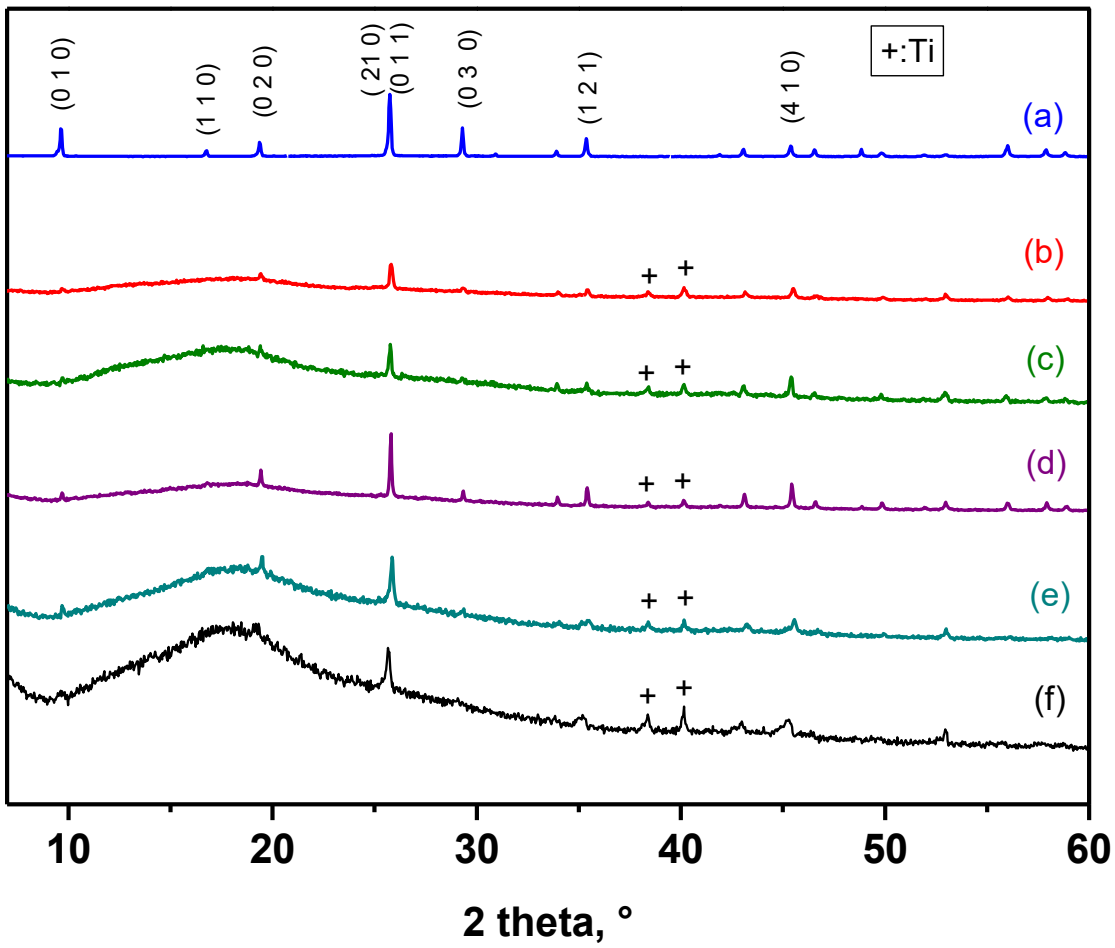

Figure 9. XRD patterns for molybdenum oxide and electrodes. (a) Pristine h-MoO_3, (b) electrode discharged to -1.5 V, (c) discharged to -1.5 V and charged to +1.5 V, (d) charged to +2.0 V, (e) discharged to -1.5 V and charged to +2.0 V, (f) after the discharge number 67. Mass ratio A.C.:h-MoO_3 = 3.0 : 1.0. The Miller indexes of the main reflections are written. The reflections of titanium foil are marked.

Table 1. Unit cell parameters of h-MoO_3 obtained by fitting the XRD patterns with the Rietveld method for an uncycled sample and full pattern matching method for electrodes retrieved from the electrochemical half cells. Mass ratio A.C.: active material=3:1. Current density: 10 mA g^{-1}. Space group $P6_3/m$. The nominal compositions are given for electrodes retrieved after the first discharge.

Sample	Lattice cell parameters
Uncycled MoO_3	a=10.5523(9) Å c=3.7246(3) Å V=359.17 $Å^3$
1st discharge (-1.5 V vs. AC), $Mg_{0.15}MoO_3$	a= 10.5500(32) Å c= 3.7303(13) Å V=359.57 $Å^3$
1st discharge-charge (-1.5 V/+1.5 V vs. AC)	a=10.5680(21) Å c= 3.7301(19) Å V=360.78 $Å^3$
1st charge (+2.0 V vs. AC)	a= 10.5536(12) Å c= 3.72576(92) Å V=359.372 $Å^3$
1st discharge-charge (-1.5 V/+2.0 V vs. AC)	a= 10.55917(86) Å c= 3.72763(61) Å V=359.934(83) $Å^3$
67th discharge (-1.5 V/+2.0 V vs. AC)	a=10.5980(51) Å c=3.760(47) Å V=365.78 $Å^3$
1st discharge (-1.5 V vs. AC in excess), $Mg_{0.67}MoO_3$	a=10.544(29) Å c=3.732(26) Å V=359.37 $Å^3$

4.8 Discussion of the reaction mechanism

Electrochemically reversible insertion of anions in inorganic materials is relatively rare. Anions use to be larger than cations and require a much greater volume. It is known that graphite, several metallorganic frameworks (MOF) and some aromatic organic compounds can be dual cation-anion electrodes [55-57]. On the other hand, it is known that high-capacity materials towards Li entail cumulative cationic ($M^{n+} \rightarrow M^{(n+1)}$) and anionic ($O^{2-} \rightarrow O_2^{2-}$) reversible redox processes [47,58]. Recently, it has been found

that anions (ClO_4^-) can be reversibly intercalated into the interlayer space of layered transition metal oxide ($Na_{0.5}Ni_{0.25}Mn_{0.75}O_2$) accompanied by an oxygen reversible redox process [59], and these authors associated this process with larger polarization and larger hysteresis than the cationic process, as we similarly observe in our results. The fundamental aspects of the anionic redox ($(O\text{-}O)^{n-}$ with n=1 ó 2) in lithium-rich and sodium-rich transition metal oxides have been explored by Yahia et al. [60]. The release of oxygen from molybdenum oxide through chemical oxidation ($O^{=}/O_2$) was reported by Guo et al. [24]. The galvanostatic method provides a method to control the extension of the redox reaction, and the partial oxidation of oxide ion in h-MoO_3 instead of releasing O_2(g). The absorption of $TFSI^-$ is concomitant to the partial oxidation of the oxide ions linked to molybdenum. On the other hand, we checked by SEM that the particle morphology was preserved ~~(figure not shown)~~, at least after the first discharge-charge cycle.

In conclusion, a significant amount of oxygen is not released from the framework of h-MoO_3 (only surface oxidation according to XPS and EPR), and conversion reaction does not happen. According to the XPS, XRD and electrochemical results, we can propose a reaction mechanism based on both reversible cation insertion and anion adsorption. A first contribution to the discharge/charge capacity must be ascribed to reversible magnesium insertion in the h-MoO_3 framework according to reaction (1). A second contribution to the reversible capacity is due to $TFSI^-$ adsorption:

$$y TFSI^- + \text{h-}MoO_3 = \text{h-}MoO_3[TFSI]_y + y e^- \quad (5)$$

Anionic (O^{2-}/O_2^{2-}) redox process in h-MoO_3 provides charge compensation for (des)insertion of $TFSI^-$ in reaction (5), over ca. 4.3 V measured vs. Mg. Simultaneously

to adsorption of $TFSI^-$ in the working electrode, the same anion is desorbed from the counter electrode. The use of anion-adsorbing A.C. as a counter electrode allows preserving the electrical neutrality in the electrolyte solution and enables the anionic redox and $TFSI^-$ adsorption in the working electrode, compared to using Mg metal as the counter electrode. Yahia et al. have proposed that the mechanism of anionic redox of transition metal oxides must involve the electron in O_{2p} orbital and violation of the octet rule [65]. We think that the covalence of the bonds between Mo(VI)-d^0 and oxygen could mitigate the violation of the octet rule. Nevertheless, the XRD results show a significant deterioration of the structure after prolonged cycling.

On the other hand, although the pristine sample h-MoO_3 only possesses a minor content of defects, it may be that the *in-situ* creation of more oxygen defects during the electrochemical charge promote pseudocapacitive behaviour. Analogously, Kim et al. reported that the oxygen vacancies previously created in chemically reduced α-MoO_3 (R-MoO_{3-x}), enlarge the interlayer spacing and induced the promoted faster pseudocapacitive energy storage kinetics in R-MoO_{3-x} employed in lithium battery [12, 61].

4.9 Rising the capacity

The results shown above serve as a proof of concept and to unveil the interesting and complex reaction mechanisms, but the electrochemical behavior of h-MoO_3 should be improved with further investigations. Thus, for that purpose the electrochemical cell design was modified, increasing the diameter available for carbon electrode, and allowing a higher amount of A.C. but no increasing the thickness of the electrode for avoiding too long diffusion length.

After increasing the mass ratio A.C.: h-MoO_3 up to 6:1, the resulting capacity at 10 mA g^{-1} is raised to around 250-350 mAh g^{-1} (Fig. 10) compared to lower A.C. mass. The capacity is increased in both the two voltage regions (charge below +1.5 V and over 1.5 V) (Fig. 10A). The reason for this extra capacity is that the excess of carbon minimizes the voltage shift due to A.C. and facilities anion adsorption. Another explanation of the capacity increase may be the contribution of a conversion reaction, but the observed capacity agrees well with the reduction from Mo^{6+} to Mo^{4+}, and henceforth formation of Mo metal and MgO is not expected. On the other hand, the decomposition of TSI^- can contribute to the pseudoplateau observed over ca. 3.5 V vs. Mg (Fig. 9A), although this voltage value is tentatively extrapolated from the experimental value measured against A.C. and then it should be taken with care. In addition, the creation of defects and/or oxygen vacancies could increase the pseudocapacitive charge storage [12, 61]. The XRD pattern of the electrode after the discharged (nominal composition $Mg_{0.67}MoO_3$) showed that the structure is preserved and the change of the lattice parameters is negligible (Table 3), although the reflections become more broadened towards lower angles. The rapid capacity fade (Fig. 10B) is in line with only partial reversibility of the charge capacity, and it is related to electrolyte decomposition, oxidation of the electrode surface and oxygen evolution. Thus, the higher capacity that is achieved by using further excess of A.C. can drive to rapid capacity fade. The results illustrate that it is necessary to develop new electrolytes for full magnesium batteries and further optimization of the cell design.

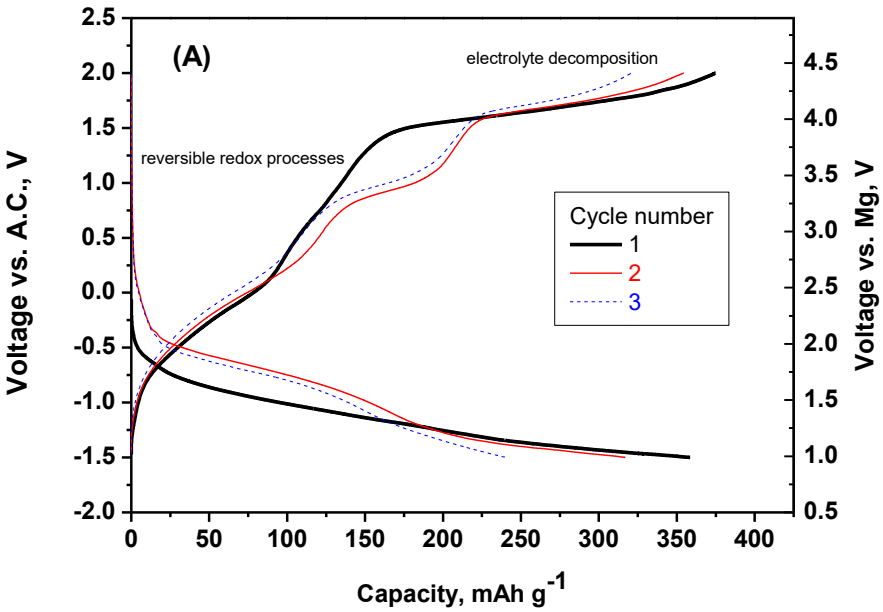
(A)
electrolyte decomposition
reversible redox processes
Cycle number
1
2
3
Voltage vs. A.C., V
Voltage vs. Mg, V
Capacity, mAh g-1

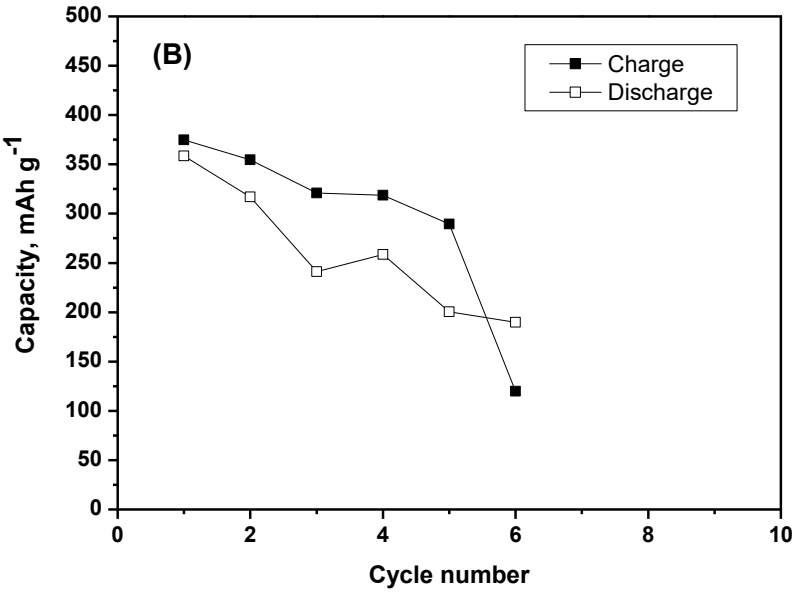
(B)
Charge
Discharge
Capacity, mAh g-1
Cycle number

Figure 10. Electrochemical behavior of h-MoO_3 vs. A.C in magnesium cell with a higher relative amount of A.C. (mass ratio A.C.: h-MoO_3 = 6.0: 1.0). Current density: 10 mA g^{-1}.

4. Conclusions

Molybdenum trioxide with hexagonal structure has been prepared and studied as an electrode for magnesium batteries. The theoretical calculation concludes that magnesium can be placed in the borders of the tunnels (6h site). However, the experimental capacity of h-MoO_3 vs. Mg metal is very limited because of the effects of the electrolyte solution on the electrode materials. The total capacity can be increased by adsorption of the anion ($TFSI^-$), particularly using activated carbon as a counter electrode, which enables that $TFSI^-$ can be reversibly adsorbed in both the positive and negative electrode, while the electrical neutrality of the solution is maintained. The layer of $TFSI^-$ can slow down the diffusion of magnesium ion into h-MoO_3. This strategy of dual cation/anion insertion (or adsorption) can provide enhancement of the total capacity. Besides the pair redox Mo^{6+}/Mo^{4+}, oxygen atoms in h-MoO_3 also contribute to the redox reaction through a pseudocapacitive-like behaviour. These results are an example of how strongly the counter electrode can influence on the apparent electrochemical behavior of the working electrode in magnesium batteries, and that the reaction mechanism can deviate from the theoretical calculations and the usual path.

Acknowledgments

The authors are grateful to *Ministerio de Economía, Industria y Competitividad* (MINECO, MAT2017-84002-C2-1-R), ERDF funds and *Junta de Andalucía* for financial support (group FQM288). We also thank SCAI-UCO for instrument facilities (XPS, FTIR, TEM, and SEM).

References

1. M.S. Whittingham, C. Siu, J. Ding. Can multielectron intercalation reactions be the basis of next generation batteries? Acc. Chem. Res. 51 (2018) 258.
2. P. Canepa, G.S. Gautam, D.C. Hannah, R. Malik, M. Liu, K.G. Gallagher, K.A. Persson, G. Ceder. Odyssey of Multivalent Cathode Materials: Open Questions and Future Challenges. Chem. Rev. 117 (2017) 4287.
3. S.C. Lim, J. Lee, H.H. Kwak, J.W. Heo, M.S. Chae, D. Ahn, Y. H. Jang, H. Lee, S.T. Hong. Unraveling the magnesium-ion intercalation mechanism in vanadium pentoxide in a wet organic electrolyte by structural determination. Inorg. Chem. 56 (2017) 7668.
4. R. Mohtadi, F. Mizuno. Magnesium batteries: Current state of the art, issues and future perspectives. Beilstein J. Nanotechnol. 5 (2014) 1291.
5. S.Y. Ha, Y.W. Lee, S.W. Woo, B. Koo, J.S. Kim, J. Xho, K.T. Lee, N.S. Choi. Magnesium(II) bis(trifluoromethane sulfonyl) imide-based electrolytes with wide electrochemical windows for rechargeable magnesium Batteries. ACS Appl. Mater. Interfaces 6 (2014) 4063.
6. D. Aurbach, Z. Lu, A. Schechter, Y. Gofer, H. Gizbar, R. Turgeman, Y. Cohen, M. Moshkovich, E. Levi. Prototype systems for rechargeable magnesium batteries. Nature 407 (2000) 407.

7. J. Song, M. Noked, E. Gillette, J. Duay, G.W. Rubloff, S.B. Lee. Activation of MnO_2 cathode by water-stimulated Mg^{2+} insertion for magnesium ion battery. Phys. Chem. Chem. Phys. 17 (2015) 5256.
8. G.S. Gautam, P. Canepa, W.D. Richards, R. Malik, G. Ceder. Role of structural H_2O in insertion electrodes: The case of Mg in nanocrystalline xerogel-V_2O_5. Nano Lett. 16 (2016) 2426.
9. K.W. Nam, S. Kim, S.S. Lee, M. Salama, I. Shterenberg, Y. Gofer, J.S. Kim, E. Yang, C.S. Park, J.S. Kim, S.S. Lee, W.S. Chang, S.G. Doo, Y.N. Jo, Y. Jung, D. Aurbach, J.W. Choi. The high performance of crystal water containing manganese birnessite cathodes for magnesium batteries. Nano Lett. 15 (2015) 4071.
10. G. Gershinsky, H.D. Yoo, Y. Gofer, D. Aurbach. Electrochemical and Spectroscopic Analysis of Mg^{2+} intercalation into thin film electrodes of layered oxides: V_2O_5 and MoO_3. Langmuir 29 (2013) 10964.
11. J. Zeng, Y. Yang, S. Lai, J. Huang, Y. Zhang, J. Wang, J. Zhao. A Promising High-Voltage Cathode Material Based on Mesoporous $Na_3V_2(PO_4)_3$/C for Rechargeable Magnesium Batteries. Chem. Eur. J. 23 (2017) 16898.
12. H. Wang, C. Zhu, D. Chao, Q. Yan, H.J. Fan. Nonaqueous hybrid lithium-ion and sodium-ion capacitors. Adv. Mater. 29 (2017) 1702093.
13. J. Ding, W. Hu, E. Paek, D. Mitlin. Review of hybrid ion capacitors: from aqueous to lithium to sodium. Chem. Rev. 118 (2018) 6457.
14. N. Gunawardhana, G.J. Park, N. Dimov, A.K. Thapa, H. Nakamura, H.Y. Wang, T. Ishihara, M. Yoshio. Constructing a novel and safer energy storing system using a graphite cathode and a MoO_3 anode. J. Power Sources 196 (2011) 7886.
15. R. Scholder and W. Klemm. Uber neue metallate mit sauerstoff und fluor als liganden. Angew. Chem. 66 (1954) 461.

16. W. H. McCarroll, L. Katz, R. Ward. Some ternary oxides of tetravalent molybdenum. J. Am.Chem Soc. 79 (1957) 5410.
17. H. Aritani, T. Tanaka, T. Funabiki, S. Yoshida, M. kudo, S. Hasegawa. Structure of Mo-Mg binary oxides in oxidized/reduced states studied by X-ray Absorption Spectroscopy at the Mo K edge and Mg K edge . J. Phys. Chem. 100 (1996) 5440.
18. M.E. Spahr, P. Novak, O. Haas, R. Nesper. Electrochemical insertion of lithium, sodium, and magnesium in molybdenum(VI) oxide. J. Power Sources 54 (1995) 346.
19. P. Novak, R. Imhof, O. Haas. Magnesium insertion electrodes for rechargeable nonaqueous batteries - a competitive alternative to lithium? Electrochim. Acta 45 (1999) 351.
20. Z. Ma, D.R. MacFarlane, M. Kar. Mg cathode materials and electrolytes for rechargeable Mg batteries: a review. Batteries & Supercaps 2 (2019) 115.
21. X.W. Lou, H.C. Zeng. Hydrothermal synthesis of alpha-MoO_3 nanorods via acidification of ammonium heptamolybdate tetrahydrate. Chem. Mater. 14 (2002) 4781.
22. V. Kumar, X. Wang, P.S. Lee. Formation of hexagonal-molybdenum trioxide (h-MoO_3) nanostructures and their pseudocapacitive behaviour. Nanoscale 7 (2015) 11777.
23. H.J. Lunk, H. Hartl, M.A. Hartl, M. J. G. Fait, I. G. Shenderovich, M. Feist, T.A. Frisk, L.L. Daemen, D. Mauder, R. Eckelt, A.A. Gurinov. "Hexagonal molybdenum trioxide". Known for 100 years and still a found of new discoveries. Inorg. Chem. 49 (2010) 9400.

24. J.D. Guo, P. Zavalij, M.S. Whittingham. Metastable hexagonal molybdates. Hydrothermal preparation, structure, and reactivity. J. Solid State Chem. 117 (1995) 323.
25. M. Cabello, F. Nacimiento, R. Alcántara, P. Lavela, C. Pérez Vicente, J.L. Tirado. On the applicability of molybdite as an electrode material in calcium batteries: a structural study of layer-type Ca_xMoO_3. Chem. Mater. 30 (2018) 5853.
26. J.M. Song, X. Wang, X.M. Ni, H.G. Zheng, Z.D. Zhang, M.R. Ji, T. Shen, X.W. Wang. Preparation of hexagonal-MoO_3 and electrochemical properties of lithium intercalation into the oxide. Mater. Res. Bull. 40 (2005) 1751.
27. G. S. Zakharova, C. Schmidt, A. Ottmann, E. Mijowska, R. Klingeler. Microwave-assisted hydrothermal synthesis and electrochemical studies of α- and h-MoO_3, J. Solid State Electrochem. 22 (2018) 3651.
28. G.S. Gautam, X. Sun, V. Duffort, L. F. Nazard, G. Ceder. Impact of intermediate sites on bulk diffusion barriers: Mg intercalation in $Mg_2Mo_3O_8$. J. Mater. Chem. A 4 (2016) 17643.
29. P.W. Ruch, D. Cericola, M. Hahn, R. Kotz, A. Wokaun, On the use of activated carbon as a quasi-reference electrode in non-aqueous electrolyte solutions. J. Electroanal. Chem. 636 (2009) 128.
30. S. J. Clark, M. D. Segall, C. J. Pickard, P. J. Hasnip, M. J. Probert, K. Refson, M. C. Payne. First principles methods using CASTEP. Z. Kristallogr. 220 (2005) 567.
31. Y. Song, Y. Zhao, Z. Huang, J. Zhao. Aqueous synthesis of molybdenum trioxide (h-MoO_3, α-$MoO_3.H_2O$ and h-/α-MoO_3 composites) and their photochromic properties study. J. All. Comp. 693 (2017) 1290.

32. J. Zhou, N. Lin, L. Wang, K. Zhang, Y. Zhu, Y. Qian. Synthesis of hexagonal MoO_3 nanorods and their electrochemical performance as anode materials for lithium-ion battery. J. Mater. Chem A 3 (2015) 7463.
33. I.P. Olenkova, L.M. Plyasova, S.D. Kirik. Crystal structure of hexagonal MoO_3. React. Kinet. Catal. Lett. 16 (1981) 81.
34. B. Darfuet, J. Galy. Une nouvelle structure à tunnels: $K_xV_xMo_{1-x}O_3$ (x = 0.13). J. Solid State Chem. 8 (1973) 189.
35. R.P. Joshi, J. Eickholt, L. Li, M. Fornari, V. Barone, J.E. Peralta. Machine learning the voltage of electrode materials in metal-ion batteries. ACS Appl. Mater. Interfaces 11 (2019) 18494.
36. M. Salama, I. Shterenberg, H.Gizbar, N.N. Eliaz, M. Kosa, K. Keinan-Adamsky, M. Afri, Linda J. W. Shimon, H. E. Gottlieb, D.T. Major, Y. Gofer, D. Aurbach, Unique behaviour of dimethoxyethane (DME)/$Mg(N(SO_2CF_3)_2)_2$ solutions. J. Phys. Chem. C 120 (2016) 19586.
37. J.N. Cha, B.S. Cheong, H.G. Cho. Solvation of $Mg(ClO_4)_2$ in deuterated acetonitrile studied by means of vibrational spectroscopy. J. Phys. Chem. A 105 (2001) 1789.
38. M. Salama, I. Shterenberg, L. J.W. Shimon, K. Keinan-Adamsky, M. Afri, Y. Gofer, D. Aurbach, Structural analysis of magnesium chloride complexes in dimethoxyethane solutions in the context of Mg batteries research. J. Phys. Chem. C 121 (2017) 24909.
39. R. Attias, M. Salama, B. Hirsch, Y. Gofer, D. Aurbach. Solvent effects on the reversible intercalation of magnesium-ions into V_2O_5 electrodes. ChemElectroChem 5 (2018) 3514.

40. R. Attias, M. Salama, B. Hirsch, R. Pant, Y. Gofer, D. Aurbach. Anion effects on cathode electrochemical activity in rechargeable magnesium batteries: a case study of V_2O_5. ACS Energy Lett. 4 (2019) 209.
41. X. Cao, L. Wang, J. Chen, J. Zheng. Low-cost aqueous magnesium-ion battery capacitor with commercial Mn_3O_4 and activated carbon. ChemElectroChem 5 (2018) 2789.
42. S.I. Castañeda, I. Montero, J.M. Ripalda, N. Díaz, L. Galán, F. Rueda. X-ray photoelectron spectroscopy study of low-temperature molybdenum oxidation process. J. Appl. Phys. 85 (1999) 8415.
43. X. Sun, V. Duffort, B.L. Mehdi, N.D. Browning, L.F. Nazar. Investigation of the mechanism of Mg insertion in birnessite in nonaqueous and aqueous rechargeable Mg-ion batteries. Chem. Mater. 28 (2016) 534.
44. M.D. Strømsheim, J. Knudsen, M.H. Farstad, L. Sørvik, X. Guo, H.J. Venvik, A. Borg. Near ambient pressure XPS investigation of CO oxidation over $Pd_3Au(100)$. Top Catal. 60 (2017) 1439.
45. W. Ranke. Low temperature adsorption and condensation of O_2, H_2O and NO on Pt(111), studied by core level and valence band photoemission. Surface Sci. 209 (1989) 57.
46. J. Grimblot, A.C. Luntz, D.E. Fowler. Low temperature adsorption of O_2 on Pt(111). J. Electron Spectrosc. Relat. Phenom. 52 (1990) 161.
47. M. Sathiya, G. Rousse, K. Ramesha, C.P. Laisa, H. Vezin, M.T. Sougrati, M.L. Doublet, D. Foix, D. Gonbeau, W. Walker, A.S. Prakash, M.B. Hassine, L. Dupont, J.M. Tarascon. Reversible anionic redox chemistry in high-capacity layered-oxide electrodes. Nat. Mater. 12 (2013) 827.
48. M. Labanowska. Paramagnetic defects in MoO_3 -revisited. Phys. Chem. Chem. Phys. 1(1999) 5385.

49. K. Li, S. Gao, Q. Wang, H. Xu, Z. Wang, B. Huang, Y. Dai, J. Lu. In-situ-reduced synthesis of Ti^{3+} self-doped TiO_2/g-C_3N_4 heterojunctions with high photocatalytic performance under LED light irradiation. ACS Appl. Mater. Interfaces 7 (2015) 9023.
50. J. Chen, Z. Ding, C. Wang, H. Hou, Y. Zhang, C. Wang, G. Zou, X. Ji. Black anatase titania with ultrafast sodium-storage performances stimulated by oxygen vacancies. ACS Appl. Mater. Interfaces 8 (2016) 9142.
51. W. Song, Q. Jiang, X. Xie, A. Brookfield, E. J. L. McInnes, P. R. Shearing, D. J. L. Brett, F. Xie, D. J. Riley. Synergistic storage of lithium ions in defective anatase/rutile TiO_2 for high-rate batteries. Energy Storage Mater. 22 (2019) 441.
52. E. Zhecheva, R. Stoyanova, J.M. Jiménez-Mateos, R. Alcántara, P. Lavela, J.L. Tirado. EPR study on petroleum cokes annealed at different temperatures and used in lithium and sodium batteries Carbon 40 (2002) 2301.
53. A. Varlec, D. Arcon, S. Skapin, M. Remskar. Oxygen deficiency in MoO_3 polycrystalline nanowires and nanotubes. Mat. Chem. Phys. 170 (2016) 154.
54. T. Tsumura, M. Inagaki. Lithium insertion/extraction reaction on crystalline MoO_3. Solid State Ion. 104 (1997) 183.
55. I.A. Rodríguez-P»rez, X. Ji. Anion hosting cathodes in dual-ion batteries. ACS Energy Lett. 2 (2017) 1762.
56. X. Zhou, Q. Liu, C. Jiang, B. Ji, X. Ji, Y. Tang, H.M. Cheng. Strategies towards low-cost dual-ion batteries with high performance. Angew. Chem. Int. Ed. 58 (2019) 2.
57. M.L. Aubrey, J.R. Long. A dual−ion battery cathode via oxidative insertion of anions in a metal−organic framework. J. Am. Chem. Soc. 137 (2015) 13594.
58. H. Koga, L. Croguennec, M. Ménétrier, K. Douhil, S. Belin, L. Bourgeois, E. Suard, F. Weill, C. Delmas. Reversible oxygen participation to the redox

processes revealed for $Li_{1.20}Mn_{0.54}Co_{0.13}Ni_{0.13}O_2$. J. Electrochem. Soc. 160 (2013) A786.

59. Q. Li, Y. Qiao, S. Guo, K. Jiang, Q. Li, J. Wu, H. Zhou. Both cationic and anionic co-(de)intercalation into a metal-oxide material. Joule 2 (2018) 1.

60. M.B. Yahia, J. Vergnet, M. Saubanère, M.L. Doublet. Unified picture of anionic redox in Li/Na-ion batteries. Nat. Mater. 18 (2019) 496.

61. H. S. Kim, J. B. Cook~~3~~, H. Lin, J. S. Ko, S. H. Tolbert~~1,~~, V. Ozolins, B. Dunn. Oxygen vacancies enhance pseudocapacitive charge storage properties of MoO_{3-x}. Nature Mater. 16 (2017) 454.